Improved Frequency-Domain Steady-State Modeling of the Dual-Active-Bridge Converter Considering Finite ZVS Transition Time Effects

Michael D'Antonio, *Graduate Student Member, IEEE*, Shiladri Chakraborty, *Member, IEEE*, and Alireza Khaligh, *Senior Member, IEEE*

***Abstract*—This article presents an improved analytical modeling (IAM) approach for the dual-active-bridge (DAB) converter in the frequency-domain. Specifically, finite transition times are incorporated into the improved modeling that are significant in DAB converters operated at high frequency. The IAM approach is first motivated by comparing traditional frequency-domain modeling against realistic simulation results in LTspice. Next, the IAM approach is mathematically developed in an iterative fashion, where the conventional frequency-domain approach is used as the initialization of the operational behavior of the converter. Subsequent iterations of the IAM algorithm incorporate finite rise- and fall-times of device output capacitances based on detailed switching behavior analyses, which may considerably perturb the desired modulation parameters (i.e., phase shift and zero states). While the initially proposed IAM approach demonstrates advantages over ideal modeling, it is still shown to exhibit errors when applied to device transitions with significant nonlinearity in parasitic output capacitance. To account for this, a three-slope approximation to the switching transition is then motivated and developed, which enables significantly improved steady-state prediction accuracy. Simulation and experimental results confirm unacceptable inaccuracies associated with the conventional frequency-domain modeling across a wide range of operating conditions, alongside enhanced accuracy provided by the proposed modeling approach.**

***Index Terms*—Dual-active-bridge (DAB), frequency-domain, steady-state modeling, zero-voltage switching (ZVS).**

I. Introduction

THE dual-active-bridge (DAB) dc–dc converter remains one of the most popular choices for bidirectional dc–dc applications due to its advantages such as the absence of turn-OFF voltage spikes across switches and possibility of full zero-voltage-switching (ZVS) operation [1]. One such realization of the DAB converter is shown in Fig. 1, with a primary-side full bridge and a secondary-side half bridge.

Manuscript received June 30, 2020; revised September 22, 2020; accepted November 17, 2020. Date of publication November 25, 2020; date of current version March 5, 2021. This work was supported by the U.S. Department of Energy's Office of Energy Efficiency and Renewable Energy under the Solar Energy Technologies Office Award DE-EE0008350. The views expressed herein do not necessarily represent the views of the U.S. Department of Energy or the United States Government. Recommended for publication by Associate Editor B. Singh. *(Corresponding author: Shiladri Chakraborty.)*

The authors are with the Department of Electrical and Computer Engineering, Maryland Power Electronics Laboratory, Institute for Systems Research, University of Maryland, College Park, MD 20742 USA (e-mail: mikey.dantonio@gmail.com; shiladri007@gmail.com; khaligh@ece.umd.edu).

Color versions of one or more figures in this article are available at https://doi.org/10.1109/TPEL.2020.3040708.

Digital Object Identifier 10.1109/TPEL.2020.3040708

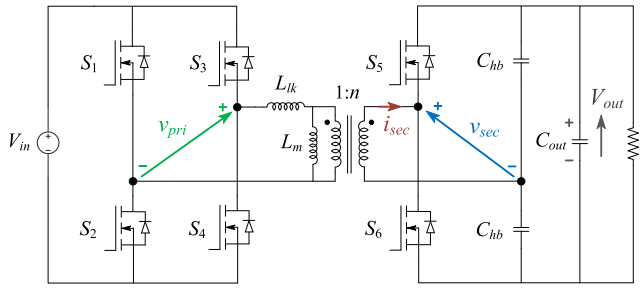

Fig. 1. DAB dc–dc converter architecture with primary-side full bridge and secondary side half bridge.

Steady-state analysis of the dc–dc DAB converter can be carried out using either time-domain modeling (TDM) or frequency-domain modeling (FDM) approaches. TDM proceeds by analyzing the circuit operation in one of several modes, which arise due to the changing voltages of the two sides of the transformer and the relative value of the modulation parameters [2]–[6]. As such, FDM was developed in [7] to significantly simplify modeling efforts into a single set of equations that are always valid. While sufficient literature has been published regarding idealized DAB circuit operation with TDM and FDM, the principle limitation of the approaches in [2]–[7] is that they neglect to consider the effect of finite rise- and fall-times (t_r, t_f) of the devices during switching transitions (cf., dotted lines in Fig. 2(b)).

A TDM approach incorporating ZVS transitions based on the state-plane analysis has been developed in [8] on a 1-MHz DAB converter. While the analysis inherently includes the impact of switching transitions, state-plane analysis of the DAB is mode dependent, which leads to nongeneric analytical descriptions of the converter. A TDM approach for predicting ZVS boundaries is presented in [9]. However, this approach is based upon achieving ZVS "by-direction" and hence, in certain instances, can prove to be inaccurate, and further does not investigate the impacts that the switching transitions have on the operational characteristics of the system. Another TDM approach is presented in [10] with accurate ZVS analyses, provided that the current at the start of the resonant transition is in the correct direction. While the impact of ZVS on the effective phase-shift perturbation is identified, the mechanisms by which this occurs and implications to

power transfer and rms currents are not present. Furthermore, this article exhibits the same limitations of complex, modally defined, time-domain analyses.

Accurate charge-based considerations for ZVS were incorporated into the FDM approach in [7]; however, the implications of ZVS transitions were not incorporated into power flow and rms current estimation. An admittance-matrix-based FDM approach for analyzing ZVS boundaries of DAB converters was presented in [11], where the ZVS boundaries are initially determined by analyzing "by-direction" considerations of the switching-leg's current, and ensuring that the current remains in the correct direction throughout the dead-time period is concluded to achieve ZVS fully. However, this will likely yield errors, for instance, if inadequate dead-time duration is provided to fully undergo the ZVS transition, or if the initial energy at the start of certain ZVS processes is insufficient. In fact, the DAB inductor current for secondary-side device transitions can begin in the wrong direction and still achieve ZVS due to the inherent behavior of the current slope [8]; these cases are not accounted for within the ZVS boundary analyses in [9]–[11].

An iteration-based time-domain approach for waveform reconstruction was necessitated in [12] for accurate system modeling and loss analysis; however, explicit details of the reconstruction method were not specified, and the implications of finite rise- and fall-times to the effective operating parameters was not explored. Therefore, considering the drawbacks of previous approaches in both the time- and frequency-domains, and the need for such a detailed modeling tool, an improved analytical modeling (IAM) approach in the frequency-domain is proposed in this article for the high-frequency dc–dc DAB converter, which could be generally extended to any other DAB-based converter approach. The contributions of this article are to: 1) create a generic model of the DAB dc–dc converter, in which the finite device commutation times are accurately considered and are applicable even in high-frequency applications; 2) analyze the impact of finite device transition times from perspectives of power transfer and rms current; 3) accurately predict the ZVS performance of all device commutations, including how much dead-time to provide to all transitions and how much residual voltage remains in quasi-ZVS (qZVS) scenarios; and 4) reconstruct time-domain wavefoRMS from the frequency-domain with high accuracy to detailed simulation and experimental results.

The rest of this article is organized as follows. Section II presents motivation for the analyses, following which the improved modeling approach is developed in Section III. Comparisons between model, simulation, and experiment are presented in Section IV. Section V presents discussion on topological applicability and benefits of the proposed approach over conventional simulation tools. Finally, Section VI concludes the article.

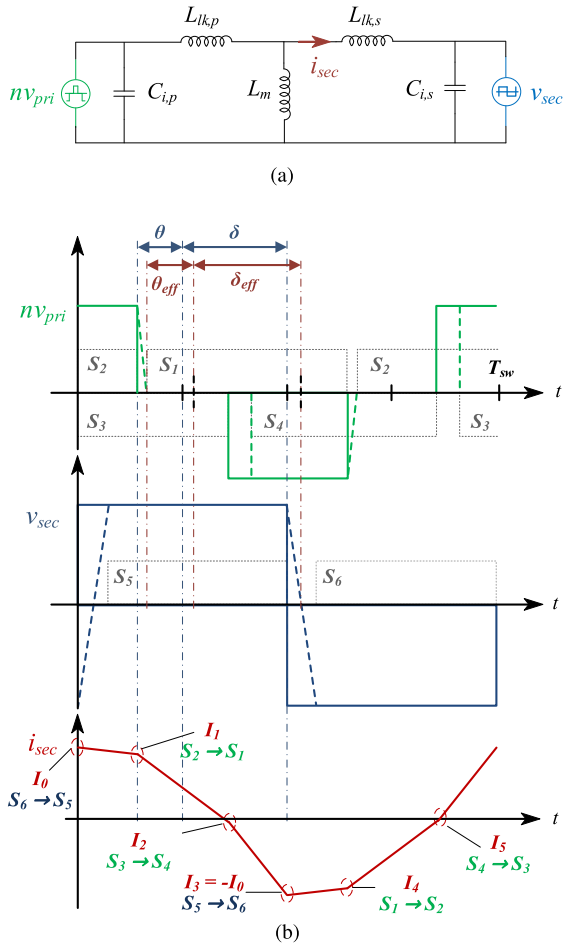

Fig. 2. DAB dc–dc converter. (a) Secondary-referred equivalent circuit. (b) Example operational waveforms. In (b), the dotted lines indicate gating waveforms of the respective devices, the solid lines demonstrate ideal waveform behavior, and the dashed lines incorporate a linearized example of finite rise- and fall-time transitions. As a result, a difference between modulator-provided δ and θ, and δ_{eff} and θ_{eff}, is realized and shown explicitly. In this case, the $S_3 \leftrightarrow S_4$ transitions are hard-switched, while $S_1 \leftrightarrow S_2$ and $S_6 \leftrightarrow S_5$ transitions are soft-switched with finite transition times, both uniquely attributing to deviation between ideal and effective modulation parameters.

II. Motivation

To motivate the necessity of an improved FDM technique, the conventional FDM approach will be developed and compared with a detailed LTspice simulation of the converter in Fig. 1. The equivalent circuit of the converter in Fig. 1, referred completely to the secondary-side of the transformer, alongside example operational waveforms is shown in Fig. 2. In the equivalent circuit shown in Fig. 2(a), the standard transformer T-model is used for inductances, in addition to transformer winding and trace-induced parasitic intrawinding capacitance on the primary- and secondary-sides. The modulation parameters are illustrated by the dashed-dotted lines in Fig. 2(b) and are defined as follows: δ is the phase-shift angle between the fundamental harmonic of the primary- and secondary-side applied transformer voltages, θ is half of the zero-state of the primary-side transformer voltage, and T_{sw} is the switching period. Henceforth, δ and θ are defined as angles in radians.

A. Conventional FDM

Traditional FDM, hereby denoted original analytical modeling (OAM), is conducted considering ideal quasi-square-wave voltages on either side of an inductive network [7], shown as solid lines in Fig. 2(a). For the equivalent circuit in Fig. 2(a),

the k-th harmonic of the primary and secondary voltages can be expressed as

$$\vec{V_{p,k}} = \frac{4nV_{\text{in}}}{k\pi}\cos(k\theta)\angle k\delta \tag{1}$$

$$\vec{V_{s,k}} = \frac{2V_{\text{out}}}{k\pi}. \tag{2}$$

Using the frequency-domain expressions for the two voltage sources, the general form of the k-th harmonic of the magnetizing inductor's voltage can be found by

$$\vec{V_{m,k}} = \vec{V_{p,k}}\Lambda_p + \vec{V_{s,k}}\Lambda_s \tag{3}$$

where $\Lambda_x = \lambda_x/(1+\lambda_p+\lambda_s)$, and $\lambda_x = L_m/L_{lk,x}$. A familiar form of this expression occurs when $L_{lk,p} = L_{lk,s}$, and $L_m \gg L_{lk,p(s)}$, in which case $\vec{V_{m,k}} = (\vec{V_{p,k}} + \vec{V_{s,k}})/2$. Using the three previous voltage vectors, the k-th harmonic of the primary- and secondary-side currents can be found via

$$\vec{I_{p,k}} = \left[\frac{\vec{V_{p,k}}}{k\omega_{\text{sw}}L_{lk,p}}(1-\Lambda_p) - \frac{\vec{V_{s,k}}}{k\omega_{\text{sw}}L_{lk,p}}\Lambda_s\right]\angle -\frac{\pi}{2} \tag{4}$$

$$\vec{I_{s,k}} = \left[\frac{\vec{V_{p,k}}}{k\omega_{\text{sw}}L_{lk,s}}\Lambda_p - \frac{\vec{V_{s,k}}}{k\omega_{\text{sw}}L_{lk,s}}(1-\Lambda_s)\right]\angle -\frac{\pi}{2}. \tag{5}$$

In order to recreate the time-domain expressions for any of these vectors, a summation of harmonics is required

$$i_x(t) = \sum_{k=1,\text{odd}}^{k_{\max}} |\vec{I_{x,k}}|\sin(k\omega_{\text{sw}}t + \angle\vec{I_{x,k}}). \tag{6}$$

Similarly, the rms currents and active power flow on the secondary can be calculated via

$$I^2_{\text{RMS},x} = \sum_{k=1}^{k_{\max}} \frac{1}{2}|\vec{I_{x,k}}|^2 \tag{7}$$

$$P_x = \sum_{k=1}^{k_{\max}} \frac{1}{2}|\vec{V_{x,k}}||\vec{I_{x,k}}|\cos(\angle\vec{V_{x,k}} - \angle\vec{I_{x,k}}). \tag{8}$$

B. Effect of Device Transitions

Due to finite rise- and fall-times of device transitions, differences can arise between the values of δ and θ set by the modulator and the operational values δ_{eff} and θ_{eff}. An example of this is highlighted by the dashed lines in Fig. 2(b), representing the voltage waveform behavior considering switching transitions with a first-order approximation. In particular, the $S_3 \leftrightarrow S_4$ transition is shown to be hard-switched, where the provided dead-time causes an increase in the effective zero-state duration. In contrast, the $S_1 \leftrightarrow S_2$ and $S_5 \leftrightarrow S_6$ transitions are shown to achieve ZVS, contributing to nonideality from another perspective. Notably, due to the finite transition speed of the secondary-side voltage, the zero-crossing (and hence the effective zero-crossing of the fundamental harmonic component) is phase-shifted from ideal considerations. Therefore, analysis of switching transition dynamics is critical to accurate predictive performance, which will be verified in the following section.

TABLE I
PARAMETERS UTILIZED IN COMPARATIVE ANALYSES

n	$L_{lk,p}$, $L_{lk,s}$	L_m	$C_{intra,p}$	$C_{intra,s}$	f_{sw}
4.28	0.6275 μH	80 μH	384 pF	22 pF	200 kHz

TABLE II
OAM VERSUS LTSPICE FOR SEVERAL DC–DC OPERATING POINTS

Case	V_{out} [V]	Analysis	δ_{eff}	θ_{eff}	I_{rms} [A]	P [W]
Sim. 1	340	OAM	0.03	0	1.61	245
		LTspice	0.045	0	2.11	328
Sim. 2	194	OAM	0.077	0.12	1.93	144
		LTspice	0.12	0.122	3.34	280
Sim. 3	107	OAM	0.093	0.19	1.67	59
		LTspice	0.12	0.191	1.33	48
Sim. 4	54	OAM	0.1	0.22	0.64	11
		LTspice	0.135	0.225	0.73	11.5

In order to illustrate the limitations of OAM in nonconsideration of device transitions, an LTspice simulation was performed, using manufacturer-supplied device models. A GaN-based EPC2001C [13] was selected for the primary-side, and a Si-based IPD60R180P7 [14] was selected for the secondary-side. The dead-times provided to the primary- and secondary-side switches were 100 and 600 ns, respectively. The remaining system parameters are listed in Table I.

Four cases were considered, where in each case the input voltage was set to 40 V and the output voltage was varied. The control parameters δ and θ were fed to a modulator from a controller, providing the appropriate gating signals to the devices. The results are presented in Table II. It is clear that there are nonnegligible differences between the rms current and power transfer values predicted by OAM [calculated with (7) and (8)] and those observed in simulation. This derives from the fact that the δ_{eff} value in simulation has been perturbed significantly from the expected δ that was provided to the system [cf., Fig. 2(b)]. Notably, the θ parameter has not differed much between the expected value and the simulation. In this case, perturbation of δ is more prominent than θ due to low required dead-time of the GaN-based EPC2001C devices and hence low ratio of dead-time to switching period in instances of soft switching, whereas the secondary-side Si devices require a longer dead-time for device commutation. While the perturbation of δ could be managed through the use of a closed-loop controller, it is important in the design and analysis stage of the converter to be able to accurately replicate expected behavior, particularly with regard to ZVS range (impacting switching losses) and rms currents (impacting conduction losses).

III. IAM APPROACH

A. Switching Transition Circuit Modeling

To accurately model converter functionality by incorporating finite-time-duration switching transitions, careful transition analysis is required. A generalized form for transition analysis in DAB converters was developed in [15] based on the equivalent

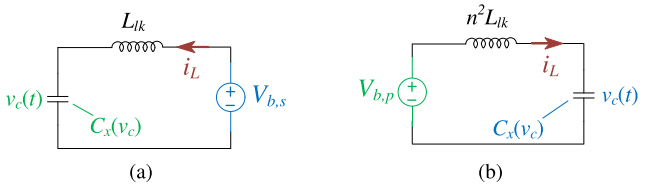

Fig. 3. Equivalent circuit model for a ZVS transition on the (a) primary-side and (b) secondary-side.

TABLE III
ZVS EQUIVALENT CIRCUIT PARAMETERS FOR FIG. 3

Transition	V_b	Cond.	C_x
$S_1 \to S_2$	$V_{out}/2n$	$\delta > \theta$	$C_{o,p}(V_{in} - V_c)+$
	$V_{out}/2n$	$\delta < \theta$	$C_{o,p}(V_c) + C_{i,p}$
$S_3 \to S_4$	$V_{out}/2n$	$\delta > \theta$	$C_{o,p}(V_{in} - V_c)+$
	$-V_{out}/2n$	$\delta < \theta$	$C_{o,p}(V_c) + C_{i,p}$
$S_6 \to S_5$	nV_{in}	$\delta > \theta$	$C_{o,s}(V_{out} - V_c)+$
	0	$\delta < \theta$	$C_{o,s}(V_c) + C_{i,s}$

circuit in Fig. 3, where $C_x(v_c)$ is the total parasitic capacitance involved in the commutation interval as a function of the capacitor voltage, $L_{lk,x}$ is the DAB power transfer inductance reflected completely to the primary or secondary sides ($x = \{p, s\}$), and $V_{b,\bar{x}}$ is an equivalent voltage source from the opposite side of the transformer (where $\bar{x} = s$ if $x = p$, and vice versa). By analyzing all possible transition scenarios, distinct values for the equivalent circuit parameters can be found as a function of the modulation parameters, summarized in Table III. Revealed in Table III is a dependence of V_b on the operating mode for transitions $S_3 \to S_4$ and $S_6 \to S_5$. While only two modes exist considering δ and θ control, many modes exist in secondary-side full-bridge realizations with an additional zero-state control [4], as well as control implementations that consider leg-level duty cycle [16]. As such, the principal limitations of previous TDM-based approaches are identification of the circuit's operating mode and solving the appropriate set of equations. In contrast, the proposed approach will be shown to have no dependence on operational modes.

B. Switching Transition Scenarios

Within any switching transition, three distinct possibilities may occur: 1) full ZVS in Fig. 4(a) and (e); 2) qZVS in Fig. 4(b), (c), (f), and (g); and 3) hard switching in Fig. 4(d). For either ZVS or qZVS transitions to occur, the transformer current must be in the correct direction to begin to discharge the parasitic output capacitance (e.g., $I_{Llk,s} > 0$ for $S_6 \to S_5$ transition). With that being said, it is possible for the current to start in the wrong direction before a current zero-crossing into the correct direction, deemed t'_x, initiating the resonant transition. In these cases, a period of third-quadrant device conduction would occur before the parasitic capacitor charging/discharging process. As such, these transitions are deemed delayed-ZVS (d-ZVS) or delayed-qZVS (d-qZVS) transitions shown in Fig. 4(e)–(g).

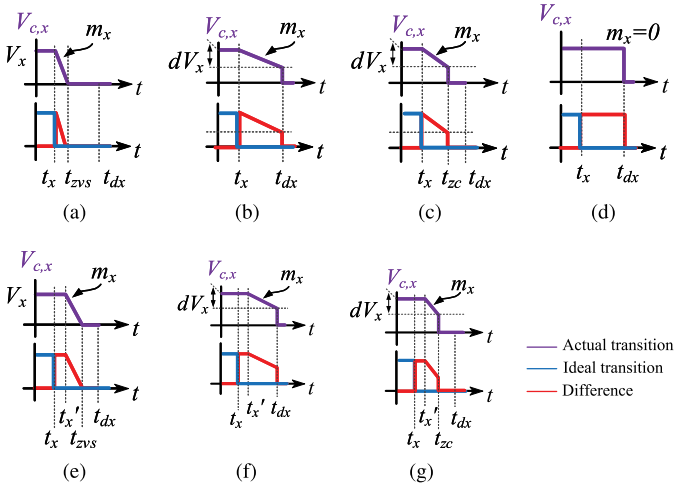

Fig. 4. Different voltage transition scenarios following the turn-OFF of a switch. (a) ZVS, (b) qZVS-TR, (c) qZVS-ER, (d) hard switching, (e) d-ZVS, (f) d-qZVS-TR, and (g) d-qZVS-ER. Actual voltage transitions are shown in purple, ideal transitions in blue, and the difference between them in red.

Combining the equivalent circuit in Fig. 3 with the appropriate parameters $V_{b,\bar{x}}$, $L_{lk,x}$, and C_x, the total time required for a full ZVS transition, with an initial transformer current $I_{L,0} = i_x(t_x)$, can be calculated via

$$t_{\text{zvs}} = \int_0^{V_x} \frac{C_x(v_c)dv_c}{\sqrt{I_{L,0}^2 + \frac{2}{L_{lk,x}} \int_0^{v_c} C_x(v)(V_{b,\bar{x}} - v)dv}} \tag{9}$$

derived in [15]. The value of time-equivalent capacitance $C_{\text{eq},t}$ can then be calculated by numerically solving

$$t_{\text{zvs}} = C_{\text{eq},t} \int_0^{V_x} \frac{dv_c}{\sqrt{I_{L,0}^2 + \frac{C_{\text{eq},t}}{L_{lk,x}} (2V_{b,\bar{x}} v_c - v_c^2)}}. \tag{10}$$

The previous equations facilitate a linear approximation to the nonlinear voltage commutation using a fixed value time-equivalent capacitance, where the equivalent capacitor's voltage rises from 0 to V_x in the time duration t_{zvs}.

The borderline between ZVS and qZVS is determined by both time- and energy-related constraints. In many circumstances, it is appropriate to select a maximum allowable amount of dead-time, t_{dx}, which will determine the borderline between ZVS and qZVS from a time-related perspective (qZVS-TR). These cases are shown in Fig. 4(b) and (f). In contrast, the inductor current may exhibit a zero crossing into the wrong direction during the switching transition due to insufficient initial energy (qZVS-ER), where the capacitor voltage would subsequently rise if the provided dead-time is too long. These cases are shown in Fig. 4(c) and (g), where t_{zc} is defined as the current zero-crossing time. In general, the qZVS transition type in Fig. 4(c) is the most generic transition form as it contains all of the other top-row cases with appropriate adjustment of t_{zc} and dV_x. For example, the ZVS case can be realized by setting $t_{zc} = t_{\text{zvs}}$ and $dV_x = V_x$. To realize any of the bottom row cases, Fig. 4(d) can be used for $t \in [t_0, t'_x]$, in cascade with Fig. 4(c) for $t \in [t'_x, t_{dx}]$.

In the cases of time- and energy-related qZVS and d-qZVS, postprocessed corrections to (9) are required.

1) Time-Related qZVS: In the case that the t_{zvs} result from (9) is greater than the designated maximum allowable dead time, a qZVS-TR situation is present. The value of dV_x can be calculated by solving the differential equations corresponding to Fig. 3 using the linear time-equivalent capacitor in (10), with the solution given by the following equations:

$$dV_x = V_{b,\bar{x}} - A_t \omega_{\text{eq},t} \cos(\omega_{\text{eq},t} t_f + \phi_t) \tag{11}$$

$$\omega_{\text{eq},t} = (L_{lk,x} C_{\text{eq},t})^{-1/2} \tag{12}$$

$$A_t = \sqrt{I_{L,0}^2 + \left(\frac{V_{b,\bar{x}}}{L_{lk,x}\omega_{\text{eq},t}}\right)^2} \tag{13}$$

$$\phi_t = \arctan\left(\frac{\omega_{eq,t} L_{lk,x} I_{L,0}}{V_{b,\bar{x}}}\right). \tag{14}$$

Using (11)–(14) with final time $t_f = t_{dx}$, all parameters are known for the linear approximation to this transition, as shown in Fig. 4(b) and (f).

2) Energy-Related qZVS: If the energy at the start of the device commutation is insufficient to facilitate full ZVS, (9) will return a real plus imaginary time result. The physical meaning of the real part to the solution is that the equivalent parasitic capacitor voltage will properly discharge in the time-shifted bound $t' \in [0, \Re(t_{\text{zvs}})]$, where $t' = t - t'_x$. However, if additional dead-time is provided to the devices, the inductor current will cross zero in the wrong direction causing the capacitor voltage to increase back toward V_x, incurring suboptimal qZVS losses. While the real part of the solution can be used to determine $t_{zc} = \Re(t_{\text{zvs}})$, the amount of voltage that has commuted during this time, dV_x, needs to be determined, which requires solving (11)–(14), with $t_f = \Re(t_{\text{zvs}})$.

3) General Transition Analysis: In order to circumvent the nongenerality between time- and energy-related qZVS transitions in the utilization of (9), and enable more complex transition modeling, a discrete solving method is utilized, adapted from the approach introduced in [17]. The block diagram for solving the switching transitions is shown in Fig. 5. The analysis begins with input of the side of the transition of interest, x, the initial time of the transition, t_x, the maximum allowable time for the transition, t_{dx}, and the total voltage of the commutation, V_x. First, it is verified that the current direction is proper to enable a resonant transition, where it is henceforth assumed that a positive current is the correct polarity. If the current is not positive, the algorithm proceeds by determining if the current crosses into the correct direction during the allowable duration of the switching transition. In instances of proper initial current direction, or in delayed transitions, the algorithm continues to the discrete solving block; otherwise, the transition is deemed to be hard-switched. In the subsequent discrete solving block for the switching commutation, the capacitor voltage v_c is stepped through in sufficiently small ΔV steps, where the total time duration of the transition, t_{tr}, and instantaneous value of inductor current, i_L, are linearly solved in each step according to

$$v_c = v_c + \Delta V \tag{15}$$

$$t_{tr} = t_{tr} + C_x(v_c)\Delta V / i_L \tag{16}$$

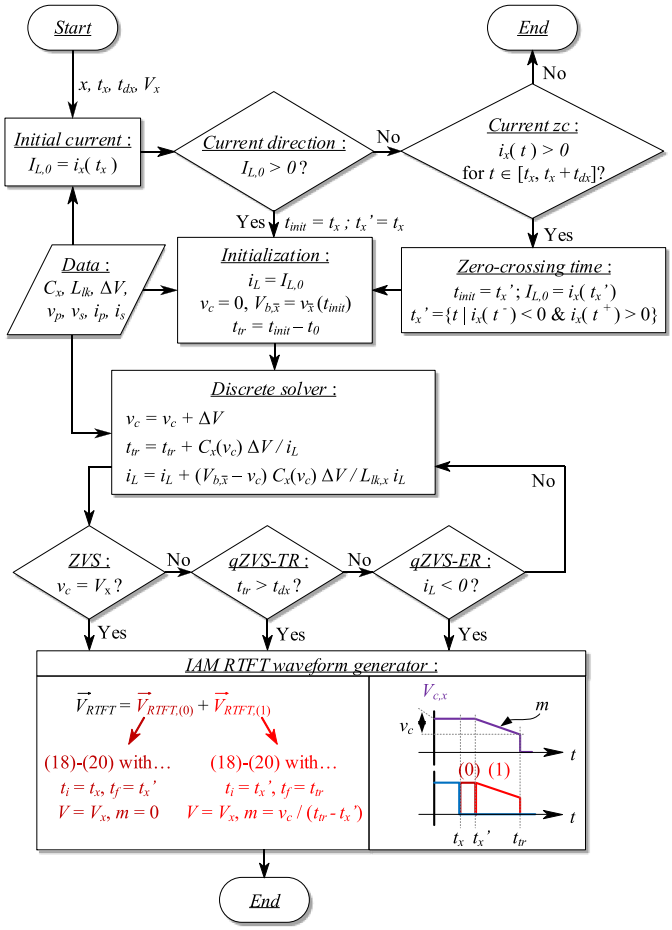

Fig. 5. Discrete solver for diagnosing switching transition types and finding the required parameters for waveform synthesis via the mathematical modeling.

$$i_L = i_L + (V_{b,\bar{x}} - v_c) C_x(v_c) \Delta V / i_L L_{lk,x} \tag{17}$$

derived as the discrete equivalent forms of the differential equations associated with Fig. 3. Therefore, in each step, violation of time-related ($t_{tr} > t_{dx}$) and energy-related ($i_L < 0$) constraints can be evaluated, and all parameters required to model the realized transition can be determined. The algorithm proceeds until one of the exit conditions is found, where the effective voltage transition can be modeled according to the diagnosed transition and mathematical modeling developed in the subsequent section.

C. Mathematical Framework for IAM

In order to incorporate the various transition types, as described in Fig. 4, an FDM of the voltage commutation intervals is required. The mathematical approach is pictorially shown in the bottom halves of each subfigure in Fig. 4, and in the waveform generator block in Fig. 5, where the ideal OAM vectors (in blue) are summed with the finite rise-time and fall-time (RTFT) vectors derived from the detailed transition analyses (in red), to create the equivalent voltage waveform (in purple). The RTFT vectors can be derived using Fourier decomposition, of which the result is included in the Appendix for the generic trapezoid in Fig. 4(c) with $t_x = t_i$ and $t_{zc} = t_f$.

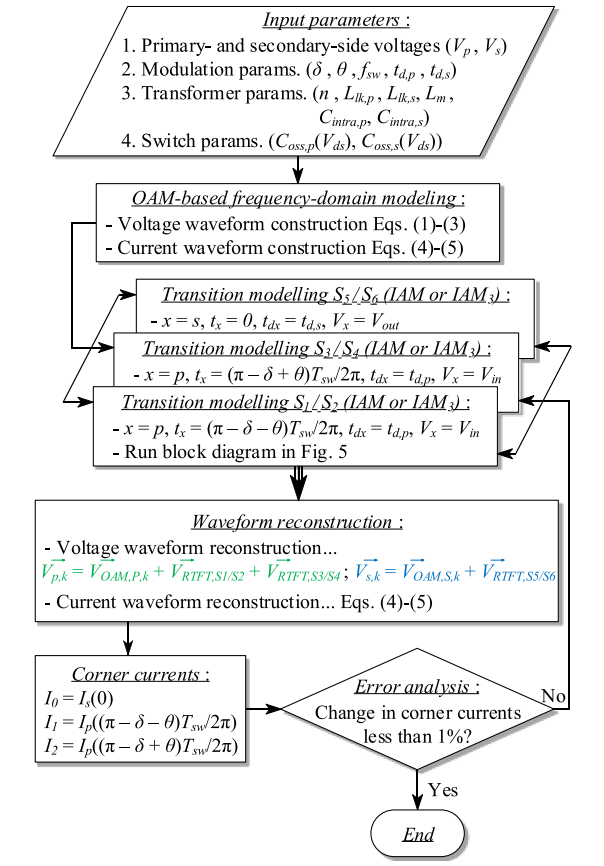

(a)

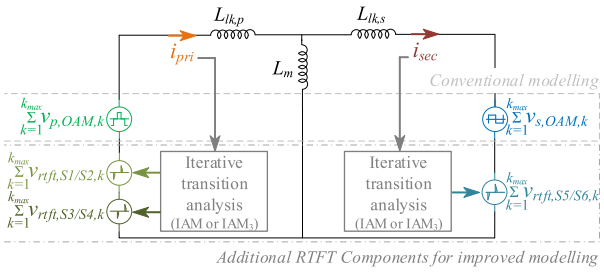

(b)

Fig. 6. Implementation of IAM incorporating finite-duration ZVS transition time effects with the conventional FDM. (a) Iterative flowchart. (b) Equivalent circuit.

With the derived mathematical formulation, it is straightforward to sum the OAM and RTFT components via vector addition. Importantly, nonnegligible magnitude and phase angle of the RTFT vectors can be present in low-order harmonics, which is the root cause in the perturbation of the effective modulation parameters.

D. Implementation

The IAM is implemented via an iterative approach, which is described by the flowchart in Fig. 6(a). In the first step, the input operating parameters are fed into the OAM equation set (1)–(5), which is used to obtain the ideal frequency-domain voltage vectors and corresponding transformer current vectors. The time-domain transformer current can be reconstructed from the frequency-domain vectors via (6), and the corner currents (i.e., the value of the transformer current at the start of the switching transition) can be utilized to perform switching transition analyses. Importantly, the switching instant times of interest, t_x, are only dependent on the modulation parameters and have no modal implications; for the proposed topology and control scheme, the primary-side transitions of interest occur at $t_p = (\pi - \delta \pm \theta)^* \, T_{\rm sw}/2\pi$, and $t_s = 0$ corresponds to the secondary-side transition of interest.[1] Eliminating modal independence of $V_{b,\bar{x}}$ is similarly straightforward, as the time-domain-reconstructed transformer voltage waveform of the side opposite to the commutation under interest can be inspected at time t_x. For example, during the $S_3 \rightarrow S_4$ primary-side transition, the secondary-side value of $V_{b,s}$ can be determined by evaluating the time-domain-reconstructed secondary-side waveform $v_s(t_x)$. With x, t_x, t_{dx}, V_x, $V_{b,\bar{x}}$, and $I_{L,0}$ known, the frequency-domain RTFT voltage vectors for each switching transition can be extracted from the detailed discrete transition analyses and waveform generator described in Fig. 5. After conducting the transition modeling for all of the switching transitions of interest, the RTFT vectors are used as correction terms via vector addition to the frequency-domain OAM voltage vectors, as explained in the previous section. The resultant modified primary- and secondary-side voltage vectors are used to reconstruct the current waveforms, which is illustrated via the modified equivalent circuit in Fig. 6(b). The iterative procedure continues until the relative change between the inductor corner currents at the current and previous iteration is uniformly less than an arbitrary error margin of 1%.

E. Limitations and Corrections

A comparison between LTspice simulation and IAM prediction is shown for one particular operating point in Fig. 7, with numerical comparison in Table IV. Unfortunately, the IAM approach detailed in previous paragraphs is shown to still result in some limitations; however, it is improved in accuracy compared to the OAM. The operating point was selected for comparison as it highlights limitations inherited in previous literature. In particular, OAM predicts the initial secondary-side corner current in the correct direction for ZVS (i.e., $I_{L,0} > 0$ at $t_s = 0$), yet when considering the effects of device commutations the current actually begins in the incorrect direction. Therefore, analyzing ZVS boundaries without considering the effect that finite-duration device transitions have on the operational characteristics of the converter may lead to inaccuracies. Nevertheless, the operation point demonstrates a case in which the secondary-side does achieve a ZVS transition, even though the initial current is in the incorrect direction.

As shown in Fig. 7, the time-based ZVS analysis is verified as the total time duration of the secondary-side ZVS transition is very closely in agreement with the simulation. This is expected by (9) because the initial resonant transition current is roughly the same in both cases; $I_{L,0} \approx 0$ as the ZVS transition

[1]For consistency of analysis, the "transitions of interest" correspond to those where the current direction shall be positive to enable a ZVS transition.

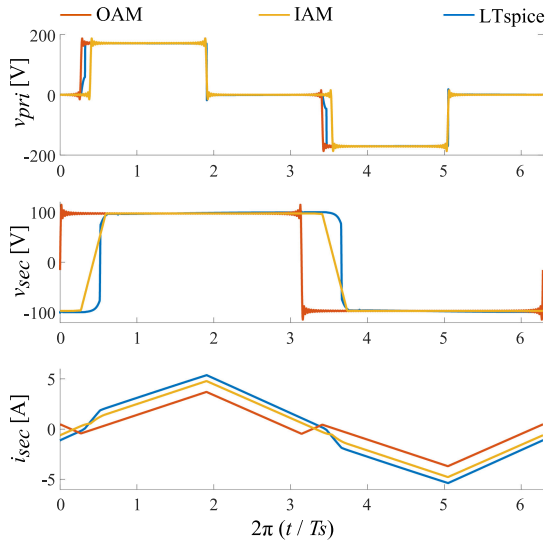

Fig. 7. Comparison for test case Sim. 2 (cf., Table II), highlighting deviation between OAM, IAM, and accurate simulation in LTspice. Error is incurred in predicting the secondary-side zero-crossing, which limits the accuracy of both the current waveform as well as predicted power flow and rms currents. Additionally, the OAM is shown to mischaracterize the circuit performance, as commutation intervals are not considered.

TABLE IV
COMPARISON OF TEST CASE SIM. 2 DC–DC OPERATING POINT

$I_{rms}[A]$			$P[W]$		
OAM	IAM	Sim.	OAM	IAM	Sim.
1.93 (42%)	2.91 (13%)	3.34	144 (48%)	240 (14%)	279.6

is initiated by a current zero-crossing. However, while the total voltage commutation time is matched closely between IAM and simulation, there is no guarantee that the final current values will also match [8], [15], [17]. Due to this, small errors in the inductor current are persistent throughout the switching period and lead to a mischaracterization of the primary-side lagging-leg transitions; IAM predicts this transition to be hard-switched, while it is qZVS-ER in simulation. The errors in power transfer and rms current are still not acceptable in this comparison, even though the results exhibit increased accuracy versus the OAM. In this case, the IAM-predicted power is less than the simulation because the IAM-predicted zero-crossing of the secondary-side waveform is earlier in time than the zero-crossing of the LTspice secondary-side waveform; hence, the δ_{eff} in IAM is less than LTspice. Therefore, it is hypothesized that the reason for the incurred error in IAM is a result of the inaccuracies associated with the linear approximation to the nonlinear secondary-side device transition. Further explanation for this alongside a proposed refinement process is outlined next.

1) Three-Step Voltage Transition: To refine the zero-crossing time of the secondary-side voltage, the ZVS transition is proposed to be broken down into a three-step piecewise linear transition. To understand the motivation behind the three-step voltage transition, an example C_{oss} versus V curve for the utilized high-voltage Si CoolMOS device is provided in Fig. 8. It is evident that after around 20 V (hereby deemed the critical

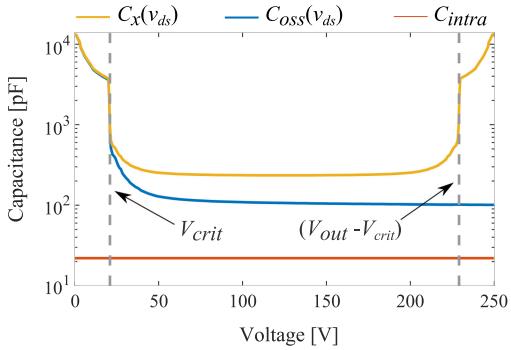

Fig. 8. Using an example Si CoolMOS device C_{oss} versus V curve to form the equivalent C_x capacitance [14]. While the device has an order of magnitude reduction at V_{crit}, the equivalent capacitance C_x experiences this behavior at both V_{crit} and $V_{\text{out}} - V_{\text{crit}}$, due to the charging and discharging behaviors of the two devices in the switching leg.

voltage, $V_{\text{crit},x}$), the parasitic capacitance experiences an order of magnitude step reduction due to completion of the channel depletion process [18]. Due to this, typically more time is required to charge and discharge the parasitic capacitance in the high-capacitance regions (cf., the shape of the secondary-side voltage in Fig. 7). Notably, two high-capacitance regions exist in the equivalent capacitance C_x, due to the charging and discharging behavior of the two devices in the switching leg (i.e., $C_x = C_{\text{oss}}(v_{ds}) + C_{\text{oss}}(V - v_{ds}) + C_{\text{intra}}$). Provided that the output voltage is larger than twice the critical voltage, three unique commutation sections can be modeled, namely: 1) $0 \rightarrow V_{\text{crit},x}$; 2) $V_{\text{crit},x} \rightarrow (V_{\text{out}} - V_{\text{crit},x})$; and 3) $(V_{\text{out}} - V_{\text{crit},x}) \rightarrow V_{\text{out}}$. In the case that the output voltage is less than twice the critical voltage, or in instances where the capacitance versus voltage characteristic is more smooth, the single-slope approximation suffices. Importantly, this three-step model is device specific, and the critical voltage may differ depending on both device technology and internal device structure. In contrast to the considered Si CoolMOS device, the EPC2001C GaN-based device utilized on the primary side has significantly reduced nonlinearity, and hence, the single-slope approximation in IAM is sufficient.

To model the three-section, piecewise linear, voltage transition, hereby denoted IAM_3, the discrete approach introduced in Fig. 5 can be adapted to analyze and model the voltage commutation in each of the three voltage regions independently. Specifically, the exit logic and waveform generator blocks presented in Fig. 5 can be modified, as shown in Fig. 9, where information regarding the time elapsed and capacitor voltage is stored in up to three unique sections, S. Regardless of the current section, conditions regarding qZVS-TR and qZVS-ER are evaluated and serve as exit conditions alongside the completion of full ZVS. The IAM_3 waveform generator is similar to that from IAM, where the single-slope RTFT vector in IAM, $V_{\text{RTFT},(1)}$, is replaced by a summation of up to three unique RTFT vectors, one for each section that was reached. An example equivalent voltage commutation in the time-domain of the three-step voltage modeling approach under the d-ZVS case is shown in the bottom of the IAM_3 waveform generator block in Fig. 9, where four trapezoidal regions are positioned appropriately to construct the dynamic voltage profile.

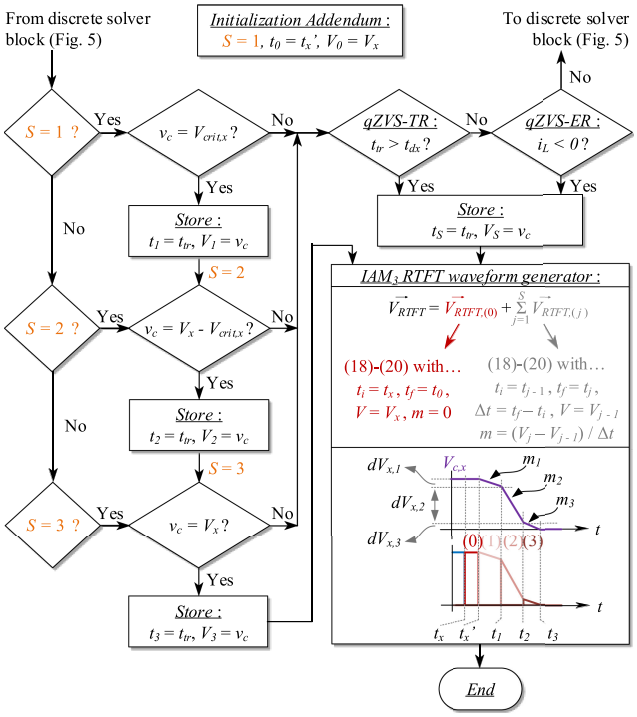

Fig. 9. Adaptation of the discrete solving method for the realization of the three-slope voltage commutation.

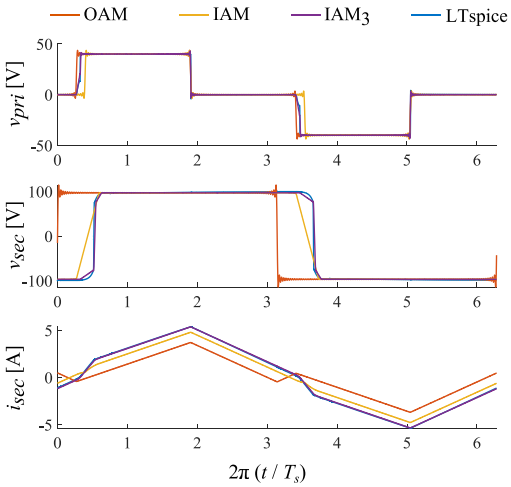

Fig. 10. Comparison of Sim. 2 operating condition between OAM, IAM, IAM_3, and LTspice.

TABLE V
REFINED COMPARISON OF THE CASE SIM. 2 OPERATING POINT

$I_{rms,IAM_3}[A]$	$I_{rms,sim}[A]$	$P_{IAM_3}[W]$	$P_{sim}[W]$
3.32 (0.61%)	3.34	278.14 (0.52%)	279.58

2) Comparison of Corrections: The simulation scenario analyzed in the beginning of this section is recompared against the IAM with the corrections outlined in the previous subsection in Fig. 10 and Table V. Notably, the primary-side devices are modeled with the single-slope approximation (IAM), whereas the secondary-side device transitions are modeled with the three-slope approximation (IAM_3). It is evident that the IAM_3 corrections to the secondary-side voltage transitions bring tight accuracy between the model and LTspice simulation, both in terms of predicted rms current and power transfer, as well as the time-domain waveform recreation. Due to the highest level of accuracy using the three-step voltage transition for the secondary-side RTFT synthesis, it is henceforth considered in the following comparison sections.

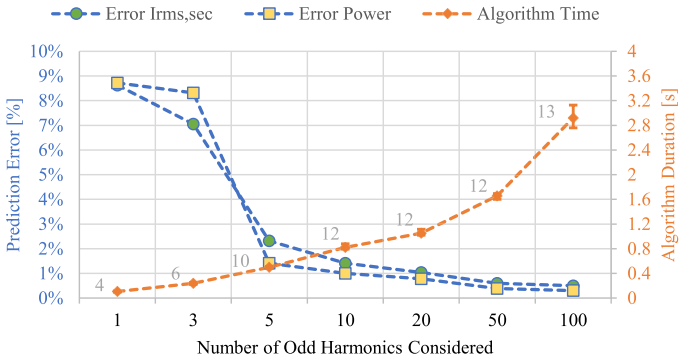

Fig. 11. Analysis of the impact of the number of harmonics for IAM_3 in example test case Sim. 2, on prediction accuracy and algorithm time duration. The total number of iterations required for convergence is shown as a data label for the algorithm duration curve.

F. Harmonic and Iterative Analysis

As with any FDM approach, the number of harmonics required to create an accurate representation of the wavefoRMS under study needs to be analyzed. Furthermore, as the proposed approach is iterative, it is important to analyze how many iterations typically are required before convergence. To analyze these two factors, the previous test condition (test case Sim. 2 in Table II) is analyzed as a function of the number of harmonics. In each case, the procedure is iterated to convergence.

The impact of the number of harmonics on the prediction accuracy of power and rms current, time duration of the algorithm, and the number of algorithmic iterations to convergence[2] is presented in Fig. 11. It is clear that the predictions of power and rms current are accurate compared to the simulated values even when considering as low as five odd harmonics. Within a 5% error bound, the algorithm converges between 10 and 13 iterations. While increases in the number of harmonics will marginally increase the prediction accuracy, increased harmonic considerations naturally come at the cost of increased execution time of the algorithm.

IV. COMPARATIVE RESULTS

A. Simulation Comparison

The remaining test conditions from Table II were compared between OAM, IAM_3, and LTspice, with the results shown in Table VI. It is clear that regardless of the modulation parameters

[2]Time measured in MATLAB R2019 on an Intel(R) Core(TM) i7-8700 CPU @ 3.20 GHz with 16-GB RAM. Algorithm runs 20 consecutive times to measure average, maximum, and minimum time durations.

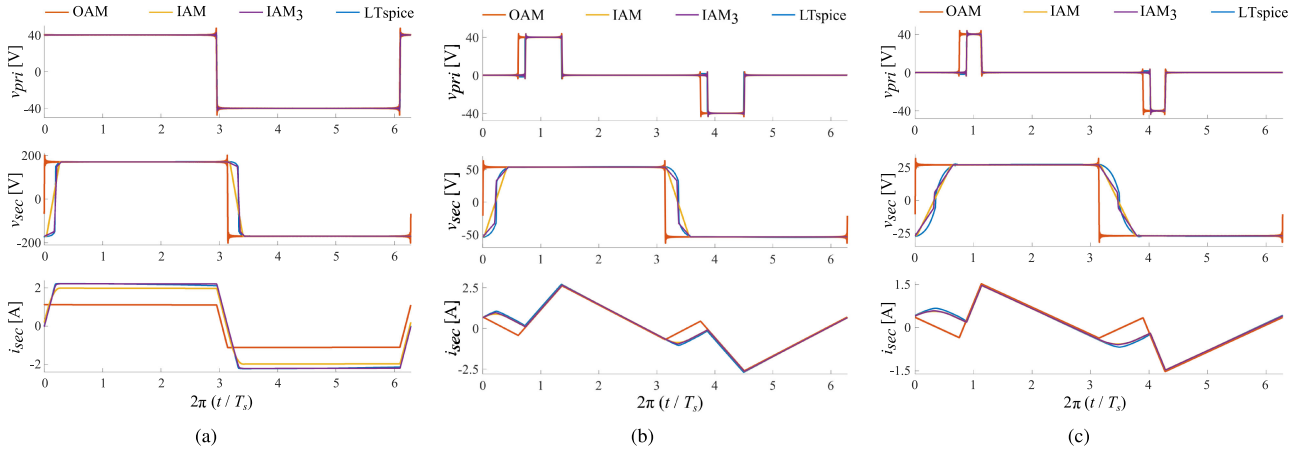

Fig. 12. Comparison of the OAM, IAM, and IAM_3 modeling approaches with LTspice simulation results for three operating conditions provided in Table II. (a) Sim. 1. (b) Sim. 3. (c) Sim. 4.

TABLE VI
COMPARISON OF MODELING APPROACHES WITH SIMULATION FOR CASES SIM. 1, 3, AND 4 FROM TABLE II

Case	$I_{rms,s}$ [A]			P [W]		
	OAM	IAM_3	LTspice	OAM	IAM_3	LTspice
Sim. 1	1.61	2.12	2.106	245	330.55	328.3
Sim. 3	1.67	1.29	1.33	59	46.9	48.1
Sim. 4	0.64	0.71	0.73	11	11.61	11.53

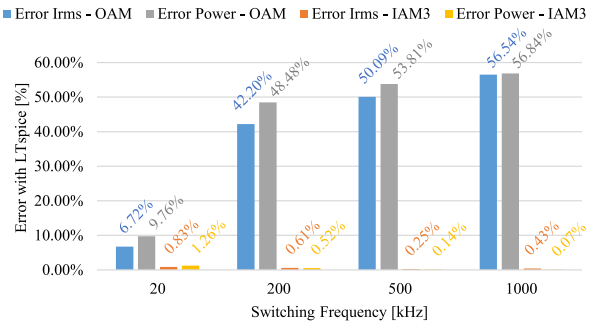

Fig. 13. Comparison of the error in rms current and power transfer between OAM and IAM_3 versus LTspice, for the Sim. 2 operating condition with wide variation in switching frequency.

and relative primary- and secondary-side voltage levels, the IAM_3 modeling approach can predict detailed LTspice performance within 5% accuracy. This is further verified in the time-domain waveforms in Fig. 12, where the LTspice results and IAM_3 predictions nearly completely overlap.

Additional simulation comparisons have been performed over a wide switching frequency range, namely f_{sw} = (20 kHz, 200 kHz, 500 kHz, 1 MHz). For comparative purposes, the Sim. 2 test case was evaluated at each switching frequency, where the inductances are each scaled according to $L_z(f_{sw}) = L_{z,nom} \cdot (200\ \text{kHz}/f_{sw})$, where $z = \{lk,p\ ;\ lk,s\ ;\ m\}$. By scaling the inductance proportional to the frequency, OAM predicts that the rms current and power transfer should remain equal in each case. Comparison of the error between OAM and IAM_3 and LTspice shown in Fig. 13 highlights the contrary. First, it should be noted that the error in OAM is within a reasonable range, $<$10% for power transfer and rms, as the switching frequency reduces to 20 kHz (i.e., the ratio of dead-time to switching period reduces such that the transitions do not affect the performance significantly). However, as the switching frequency increases, OAM is invalidated with $>$50% errors in both rms current and power transfer at high switching frequency. In contrast, the error with the proposed IAM_3 modeling approach is uniformly less than 2% in each of the cases. As the trend of future power electronic converters is to increase switching frequency for volume and weight advantages, use of the proposed IAM modeling is indispensable for steady-state prediction accuracy.

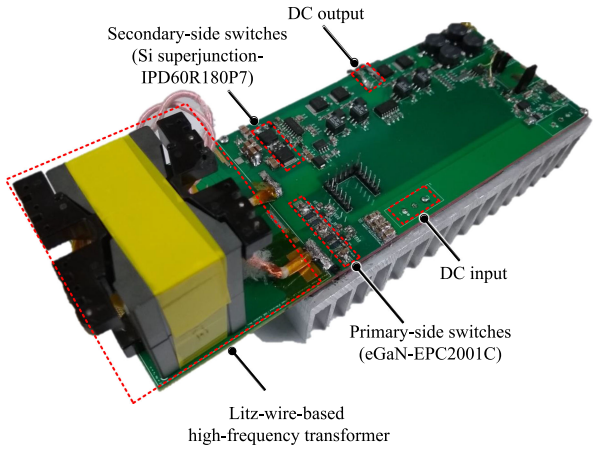

Fig. 14. Annotated photograph of the prototype used for experiments.

B. Experimental Comparison

Several dc–dc operating points have been tested in hardware with the devices considered thus far and other specifications provided in Table I. The experimental results were facilitated by the prototype shown in Fig. 14. The specifications of the

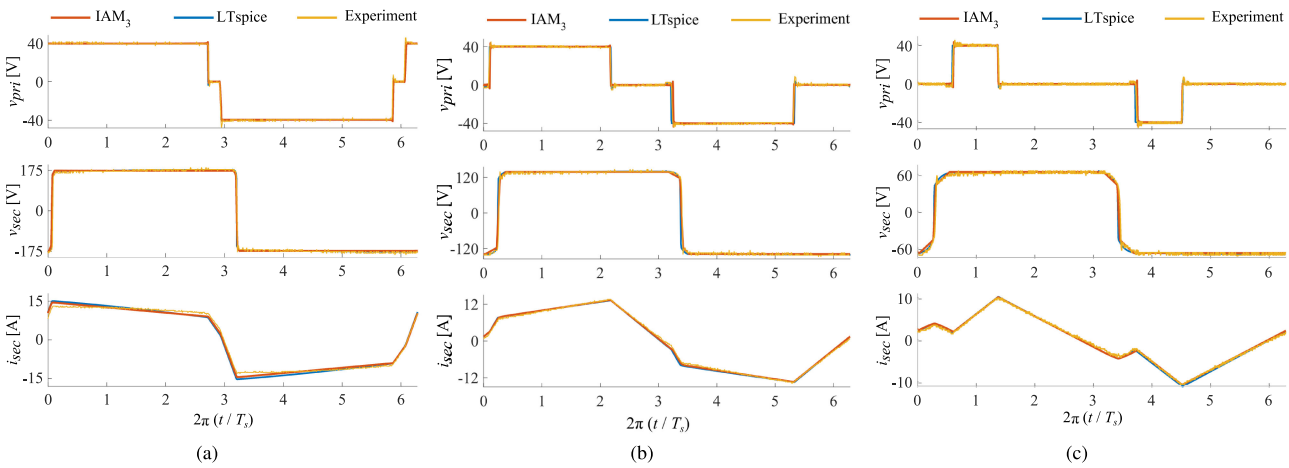

Fig. 15. Comparison of IAM_3 model predictions, LTspice simulation results, and experimental results for the three operating conditions provided in Table VII. (a) Exp. 1. (b) Exp. 2. (c) Exp. 3.

TABLE VII
VOLTAGE LEVELS AND MODULATION PARAMETERS VALUES OF THE TEST CONDITIONS IN THE EXPERIMENTAL RESULTS SECTION

Test Case	V_{in} [V]	V_{out} [V]	δ	θ	f_{sw} [kHz]
Exp. 1	39.4	345.84	0.051	0.016	149
Exp. 2	40.1	276.74	0.0797	0.0747	249
Exp. 3	39.9	131.49	0.104	0.179	249

TABLE VIII
COMPARISON OF THE OPERATING POINTS IN TABLE VII

Test #	Model	P [W] (error %)	$I_{rms,p}$ [A] (error %)
Exp. 1	OAM	358.96 (14.2%)	9.70 (13.8%)
	IAM_3	408.62 (2.3%)	11.12 (1.2%)
	LTspice	411.63 (1.6%)	11.28 (0.22%)
	Exp.	418.39	11.25
Exp. 2	OAM	215.8 (19.4%)	7.27 (22.5%)
	IAM_3	271.34 (1.3%)	9.39 (0.1%)
	LTspice	272.56 (1.8%)	9.47 (0.9%)
	Exp.	267.77	9.38
Exp. 3	OAM	54.19 (10.2%)	4.77 (14.5%)
	IAM_3	64.26 (6.5%)	5.61 (0.6%)
	LTspice	63.79 (5.7%)	5.63 (1%)
	Exp.	60.35	5.58

three tests are provided in Table VII. Of importance in comparing simulation and model results to a hardware experiment is including timing delays (propagation, rise-time, fall-time, etc.) between the controller and device gate–source voltage. With proper characterization, delay estimates can be incorporated into LTspice and IAM accordingly.[3]

The numerical results of the experimental tests were extracted using a Keysight 1-GHz bandwidth oscilloscope (DSOX4104A) for rms current measurements and a PA3000 power analyzer for power transfer measurements. The experimental results were compared against LTspice and IAM_3, with implemented timing delays, numerically in Table VIII and pictorially in Fig. 15. From the numerical results, it is clear that both the IAM_3 and LTspice are predictive of the hardware results, while the OAM exhibits undesirable error. The accuracy of IAM_3 and LTspice to the experiment both validates the simulation verification from the previous section and further necessitates the use of the proposed modeling approach. As such, the motivation for and contributions of IAM_3 are clear from the agreement between rms current and power transfer, and the accuracy of time-domain waveform generation (and hence device transition modeling) that replicates the experimental performance of the converter.

V. DISCUSSION

A. Topological Applicability

The proposed improved FDM approach considering both ideal analysis and the effects of rise- and fall-times during switching transitions can be applied for other topologies and adapted for various purposes. From a topological perspective, the proposed modeling is applicable to any topology, which can be equivalently modeled by the dual-port voltage circuit presented in Fig. 2, with an arbitrary impedance network between the two sources. This includes, but is not limited to, the three-phase DAB, resonant DAB, and nonisolated realizations of these structures. In the application of improved FDM modeling for other topologies, the principal difference is in characterization of the OAM equation set, particularly for the primary- and secondary-side voltages (which may have m-number of voltage levels) and the primary- and secondary-side currents (which will depend on the impedance network considered). Furthermore, the equivalent circuit for switching transitions may differ with a unique set of associated differential equations. Nevertheless, the differential equations according to the switching transition equivalent circuit can be discretized and solved with a similar technique utilized in the "discrete solver" section of Fig. 5. With

[3]In the model, the turn-OFF delay can be added to the start of the ZVS interval for each switch, and the difference between turn-ON and turn-OFF delay can be added to the effective device dead-time.

these two variations compared to the proposed topology, the RTFT waveform generation via IAM or IAM_3 can be utilized and summed with OAM as an error vector, similar to the approach demonstrated in Fig. 6. Therefore, while some variation may exist in the extension of the approach to other topologies, the fundamental mathematical modeling and utilization of the RTFT vectors remains the same.

B. Benefits Over Conventional Simulation Tools

Although powerful simulation tools are widely available to many power electronics designers, developing accurate analytical modeling for steady-state operation remains extremely valuable. The major justification for utilizing the proposed model is in the development of executable code, which predicts the steady-state circuit performance, even as the circuit is operated at higher switching frequency. While there are some advantages regarding the computation time of the proposed approach versus steady-state simulation models, principal benefits of the approach come in enabling optimization within numerical computing environments such as MATLAB. In comparison, parametric sweeps are available in most simulation tools; however, this requires the designer to export and subsequently analyze each of the steady-state results independently. In contrast, the proposed modeling can be used as the central block of a constrained numerical optimization function such as MATLAB "*fmincon*," as was performed for control-level optimization in [7] (minimizing rms current, while transferring desired amount of power and enabling near-uniform ZVS), and extended for design-level optimization in [19] (selection of transformer turns ratio and leakage inductance that minimizes the circuit's weighted conduction loss). On another note, the IAM approach can be utilized for accurate characterization and optimization of the circuit efficiency in steady-state, as discussed in [12], and used as an open-loop testing assist tool for circuit-level parametric characterization. In general, in line with the future trends of power electronics to operate converters at higher switching frequency, the proposed approach is indispensable to steady-state modeling accuracy of DAB-based converters.

VI. Conclusion

This article has proposed an improved FDM technique for the DAB dc–dc converter. It is demonstrated that as DAB converters are operated at higher frequency, the finite rise- and fall-times of the effective commutation capacitances during a switching transition can significantly perturb the effective modulation parameters, which can lead to inaccuracies in the predicted power transfer, rms current, and ZVS performance. As such, a detailed switching transition model was incorporated with the traditional ideal FDM in an iterative fashion. The initially proposed IAM algorithm incorporating rise- and fall-time effects with a single-slope linear approximation provided some benefits; however, it was still inaccurate in replicating performance with devices exhibiting sufficient nonlinearity in parasitic output capacitance. As such, a piecewise linear transition involving three unique sections was proposed, which was shown to match with both LTspice simulation and hardware experiments within tight error margins, over a wide range of operating conditions and switching frequencies. Finally, extensions and applications of the modeling approach were presented, demonstrating the flexibility for other topologies and optimal design analyses.

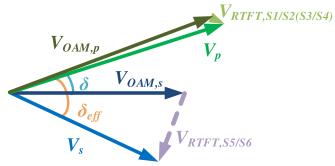

Fig. 16. Example phasor diagram at the k-th harmonic showing the summation of OAM and RTFT vectors to obtain the equivalent voltage vector on both the primary-and-secondary-sides.

Appendix

By applying Fourier decomposition of the finite rise- and fall-time waveforms, frequency-domain expression for the RTFT vectors can be derived. It is assumed that due to operational symmetry of the DAB, the devices in the same leg experience the same transition parameters, and hence, the RTFT vectors have odd symmetry and only contain odd harmonics. The results of the Fourier decomposition are summarized in the following formulas:

$$\alpha_k = \frac{2}{k^2\pi} m[\cos(kt_i) - \cos(kt_f)] + \frac{2}{k\pi} V[\sin(kt_f) - \sin(kt_i)] - \frac{2}{k\pi} m\,(t_f - t_i)\sin(kt_f) \quad (18)$$

$$\beta_k = \frac{2}{k^2\pi} m[\sin(kt_i) - \sin(kt_f)] + \frac{2}{k\pi} V[\cos(kt_f) - \cos(kt_i)] - \frac{2}{k\pi} m\,(t_f - t_i)\cos(kt_f) \quad (19)$$

$$\vec{V_{\text{RTFT},k}} = \sqrt{\alpha_k^2 + \beta_k^2}\sin(k\omega t - \arctan(\beta_k/\alpha_k)). \quad (20)$$

The summation of the OAM and RTFT vectors at an example k-th harmonic are shown pictorially in Fig. 16.

Acknowledgment

This work was supported by the U.S. Department of Energy's Office of Energy Efficiency and Renewable Energy under the Solar Energy Technologies Office Award DE-EE0008350.

References

[1] M. H. Kheraluwala and R. W. De Doncker, "Single phase unity power factor control for dual active bridge converter," in *Proc. IEEE Ind. Appl. Soc. Annu. Meeting*, Toronto, ON, Canada, 1993, vol. 2, pp. 909–916.
[2] G. Oggier, G. Garcia, and A. Oliva, "Modulation strategy to operate the dual active bridge dc–dc converter under soft switching in the whole operating range," *IEEE Trans. Power Electron.*, vol. 26, no. 4, pp. 1228–1236, Apr. 2011.
[3] F. Krismer and J. W. Kolar, "Closed form solution for minimum conduction loss modulation of DAB converters," *IEEE Trans. Power Electron.*, vol. 27, no. 1, pp. 174–188, Jan. 2012.

[4] J. Everts, F. Krismer, J. Van den Keybus, J. Driesen, and J. W. Kolar, "Optimal ZVS modulation of single-phase single-stage bidirectional DAB AC–DC converters," *IEEE Trans. Power Electron.*, vol. 29, no. 8, pp. 3954–3970, Aug. 2014.
[5] F. Jauch and J. Biela, "Combined phase-shift and frequency modulation of a dual-active-bridge AC–DC converter with PFC," *IEEE Trans. Power Electron.*, vol. 31, no. 12, pp. 8387–8397, Dec. 2016.
[6] T. Chen, R. Yu, Q. Ma, X. Zhao, and A. Q. Huang, "Optimal control scheme for single-stage dual-active-bridge AC–DC converter," in *Proc. IEEE Energy Convers. Congr. Expo.*, 2018, pp. 2860–2864.
[7] J. Everts, G. E. Sfakianakis, and E. A. Lomonova, "Using Fourier series to derive optimal soft-switching modulation schemes for dual active bridge converters," in*Proc. IEEE Energy Convers. Congr. Expo.*, 2015, pp. 4648–4655.
[8] D. Costinett, "Analysis and design of high efficiency, high conversion ratio, dc–dc power converters," Ph.D. dissertation, Dept. Elect., Comput., Energy Eng., Univ. Colorado, Boulder, CO, USA, 2013.
[9] S. S. Shah, V. M. Iyer, and S. Bhattacharya, "Exact solution of ZVS boundaries and AC-port currents in dual active bridge type dc–dc converters," *IEEE Trans. Power Electron.*, vol. 34, no. 6, pp. 5043–5047, Jun. 2019.
[10] H. Shi, H. Wen, and Y. Hu, "Deadband effect and accurate ZVS boundaries of GaN-based dual active bridge converters with multiple-phase-shift control," *IEEE Trans. Power Electron.*, vol. 35, no. 9, pp. 9886–9903, Sept. 2020.
[11] J. Riedel, D. G. Holmes, B. P. McGrath, and C. Teixeira, "ZVS soft switching boundaries for dual active bridge dc–dc converters using frequency domain analysis," *IEEE Trans. Power Electron.*, vol. 32, no. 4, pp. 3166–3179, Apr. 2017.
[12] R. M. Burkart and J. W. Kolar, "Comparative $\eta\rho\sigma$ Pareto optimization of Si and SiC multilevel dual-active-bridge topologies with wide input voltage range," *IEEE Trans. Power Electron.*, vol. 32, no. 7, pp. 5258–5270, Jul. 2017.
[13] *EPC2001C—Enhancement Mode Power Transistor*, Efficient Power Conversion Corp., El Segundo, CA, USA. [Online]. Available: https://epc-co.com/epc/Portals/0/epc/documents/datasheets/EPC2001C_datasheet.pdf, Accessed: Oct. 12, 2020
[14] *IPD60R180P7 600 V CoolMOS P7 Power Device*, Infineon Technol., Neubiberg, Germany. [Online]. Available: https://www.infineon.com/dgdl/Infineon-IPD60R180P7-DS-v02_02-EN.pdf?fileId=5546d46259d9a4bf015a5bd338b83cb3
[15] D. Costinett, R. Zane, and D. Maksimovic, "Circuit-oriented modeling of nonlinear device capacitances in switched mode power converters," in *Proc. IEEE 13th Workshop Control Model. Power Electron.*, Jun. 2012, pp. 1–8.
[16] S. Chakraborty, M. Palmal, and S. Chattopadhyay, "Approaches for continuous-time dynamic modeling of the asymmetric dual-active half-bridge converter," in *Proc. IEEE 33rd Annu. Appl. Power Electron. Conf. Expo.*, San Antonio, TX, USA, 2018, pp. 952–958.
[17] D. Costinett, D. Maksimovic, and R. Zane, "Circuit-oriented treatment of nonlinear capacitances in switched-mode power supplies,"*IEEE Trans. Power Electron.*, vol. 30, no. 2, pp. 985–995, Feb. 2015.
[18] M. Guacci *et al.*, "On the origin of the C_{oss} -losses in soft-switching GaN-on-Si power HEMTs," *IEEE J. Emerg. Sel. Topics Power Electron.*, vol. 7, no. 2, pp. 679–694, Jun. 2019.
[19] M. D'Antonio, S. Chakraborty, and A. Khaligh, "Design optimization for weighted conduction loss minimization in a dual-active-bridge-based PV microinverter," in *Proc. IEEE Energy Convers. Congr. Expo.*, 2020, pp. 6008–6015.

Michael D'Antonio (Graduate Student Member, IEEE) received the B.S. degree in electrical engineering in 2016 from the University of Maryland, College Park, MD, USA, where he is currently working toward the Ph.D. degree in electrical engineering.

His current research interests include modeling, design, and optimization of high-efficiency and high-power-density power electronic converter solutions for renewable energy, transportation electrification, and data center applications.

Shiladri Chakraborty (Member, IEEE) received the B.E. degree from Jadavpur University, Kolkata, India, in 2008, the M.Tech. degree from the Indian Institute of Technology (IIT) Kanpur, Kanpur, India, in 2012, and the Ph.D. degree from IIT Kharagpur, Kharagpur, India, in 2019, all in electrical engineering.

He is currently a Postdoctoral Associate with the University of Maryland, College Park, MD, USA. His research interests include dual-active-bridge converters, wide-bandgap semiconductor-based converters, integrated packaging of power switches, and high-frequency magnetics.

Alireza Khaligh (Senior Member, IEEE) is a Professor and the Director of Maryland Power Electronics Laboratory, Department of Electrical and Computer Engineering, the Institute for Systems Research, University of Maryland, College Park, MD, USA. He has authored or coauthored more than 200 journals and conference papers. His current research interests include modeling, analysis, design, and control of power electronic converters for transportation electrification, renewable energies, Internet of Things, and wearable electronics.

Dr. Khaligh is the Deputy Editor-in-Chief for the IEEE TRANSACTIONS ON TRANSPORTATION ELECTRIFICATION.